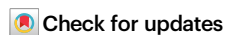


High-contrast in vivo fluorescence imaging exploiting wavelengths beyond 1880 nm

Received: 25 September 2024

Accepted: 25 April 2025

Published online: 13 May 2025

Jiayi Li^{1,4}, Qiming Xia^{2,4}, Tianxiang Wu^{1,4}, Yuhuang Zhang¹, Shiyi Peng¹, Yifei Li¹, Yixuan Li², Hui Lin², Mingxi Zhang³✉ & Jun Qian¹✉

The second near-infrared (NIR-II) window is widely acknowledged for its excellent potential in in vivo fluorescence imaging. Currently, NIR-II fluorescence imaging predominantly operates within the 900–1880 nm spectral range, while the region beyond 1880 nm has been disregarded due to the large light absorption of water. Based on a refined understanding of the effect of light absorption on imaging, we propose an approach that utilizes the previously neglected region surrounding the water absorption peak at ~1930 nm for imaging. Both simulations and experiments confirm that the water absorption contributes positively to imaging, enabling high-contrast in vivo fluorescence imaging in the 1880–2080 nm window. To further assess the applicability of this approach in different biological media, we extend our focus to fluorescence imaging in adipose tissue. This leads to the expansion of the imaging window to 1700–2080 nm, owing to the unique light absorption characteristics of adipose tissue. Our results demonstrate that the 1700–2080 nm region provides optimal imaging quality in adipose tissue, attributing to its moderate absorption and low scattering. This work advances our understanding of the interplay between light absorption and photon scattering in bioimaging, providing an insight for selecting optimal imaging windows to achieve high-contrast fluorescence imaging.

Fluorescence imaging, combining the advantages of its high temporal and spatial resolution and radiation-free properties, has a wide range of applications in the biomedical field¹. In recent years, the second near-infrared window (NIR-II, 900–1880 nm) fluorescence imaging, has gained significant attention due to its low photon scattering and reduced biological autofluorescence^{2–11}. In particular, based on the varying properties of scattering and absorption, NIR-II is divided into several specific imaging sub-windows, including NIR-IIa (1300–1400 nm), NIR-IIb (1500–1700 nm), and NIR-IIc (1700–1880 nm)^{3,12,13}. Indeed, light propagation through biological media is an essential process in fluorescence bioimaging. This

physical process is accompanied by absorption attenuation and scattering perturbations, which have conventionally been regarded as detrimental to the performance of bioimaging. As a result, a common approach improving imaging quality is to minimize scattering by increasing wavelength and avoid spectral regions with strong absorption peaks^{14–16}. However, recent studies have challenged this conventional opinion by highlighting the beneficial role of absorption in enhancing the imaging contrast^{13,17–19}. The improvement in contrast is attributed to the greater attenuation of background signals with longer optical paths in scattering media, thereby increasing the relative proportion of useful signals. This

¹State Key Laboratory of Extreme Photonics and Instrumentations, Centre for Optical and Electromagnetic Research, College of Optical Science and Engineering, International Research Center for Advanced Photonics, Zhejiang University, Hangzhou, China. ²Department of General Surgery, Sir Run Run Shaw Hospital, Zhejiang University School of Medicine, Hangzhou, China. ³State Key Laboratory of Advanced Technology for Materials Synthesis and Processing, Wuhan University of Technology, Wuhan, China. ⁴These authors contributed equally: Jiayi Li, Qiming Xia, Tianxiang Wu.

✉ e-mail: mxzhang@whut.edu.cn; qianjun@zju.edu.cn

insight has led to a deeper understanding and reevaluation of the NIR-II window. Notably, the NIR-IIx (1400–1500 nm) region, previously disregarded due to the water absorption peaks, has demonstrated unique advantages in terms of imaging contrast and relative depth^{13,20} when the fluorescent probe is bright enough. Similarly, the third near-infrared window (NIR-III, 2080–2340 nm), which exhibits similar water absorption property, has been proposed as a promising imaging window¹³. Nevertheless, imaging studies are absent near 1930 nm because the huge water absorption peak at ~1930 nm was regarded as an insurmountable barrier.

Giving the positive impact of light absorption in tissues in NIR-II fluorescence imaging, previously dismissed regions with high water absorption may show potential for exceptional imaging performance. The excellent imaging capabilities of the NIR-IIx window^{13,20} have inspired the exploration of spectral bands with greater absorption. Recent advancements in bright fluorescent probes with peak emission wavelength beyond 1500 nm have significantly contributed to the development of NIR-IIb and NIR-IIc fluorescence imaging, paving the way for further exploration of longer wavelength windows^{21–24}. When the signal intensity sufficiently compensates for absorption attenuation, the underexplored 1880–2080 nm window whose starting point and endpoint are established based on the peak absorption coefficient of water in NIR-IIx region may demonstrate superior imaging potential due to enhanced scattering suppression from wavelength redshift and increased water absorption. Furthermore, absorption characteristics vary across different biological components¹¹. For example, water and adipose tissue have distinct absorption peaks^{25–27}. To date, the key challenge still lies in identifying optimal imaging windows for different tissue environments.

In this study, we aimed to find more suitable imaging windows in complex biological environments by integrating the effects of light absorption and photon scattering on imaging quality. By using Monte Carlo simulation to model the propagation of photons in biological tissues, we investigated how light absorption can improve the imaging performance and explored potential high-quality windows for near-infrared fluorescence imaging. Notably, we proposed that the 1880–2080 nm band, with imaging properties comparable to NIR-IIx window, offered higher contrast imaging when water absorption attenuation was sufficiently overcome. Consequently, high-quality *in vivo* fluorescence imaging was realized in the 1880–2080 nm band using water-soluble core-shell PbS/CdS quantum dots (QDs), which emitted bright fluorescence at long wavelength. Moreover, the effects of absorption became particularly significant in scenarios with large background interference from deeper tissue regions. For example, when imaging the skin vessels above the mouse liver, the 1880–2080 nm and NIR-IIx regions showed distinct advantages due to enhanced absorption, while other NIR-II sub-windows struggled to distinguish target signals from the background noise. To further explore the potential of the 1880–2080 nm band, we employed both this band and NIR-IIx window for multi-channel bioimaging. Additionally, the selection of optimal imaging windows for complex biological tissues requires further optimization based on scattering and absorption theories. In particular, our study examined adipose tissue, a major component of the human body, which has different optical parameters. Simulations revealed that the unique light absorption and the low photon scattering in adipose tissue, which contributed to the best imaging performance in the band of 1700–2080 nm. This result was further supported by both *in vitro* and *in vivo* experiments.

Results

Simulation and exploration of near-infrared fluorescence bioimaging based on light absorption and photon scattering of tissues

Photons are affected by scattering and absorption as they propagate through biological tissues. It was previously accepted that both

scattering and absorption lead to the deterioration of image quality, as they result in a loss of information. However, the mechanisms and consequences of scattering and absorption are not the same¹⁷. On one hand, scattering blurs the image because photons that initially propagate to the same pixel scatter to multiple pixels. In NIR-II bioimaging studies, it has been emphasized to suppress scattering by increasing wavelength. On the other hand, absorption attenuates the intensity of the signal received by the detector, which in the past was known to reduce the signal-to-noise ratio. However, the interfering background from scattered signal photons is preferentially depleted while absorbing signal photons, because the path length of multiply scattered photons is much longer than that of ballistic signal photons. This leads to an increase in the proportion of ballistic photons arriving at the detector (Fig. 1a), which improves the signal-to-background ratio (SBR) of image. In addition, the attenuation of signal caused by absorption can be compensated for by other methods such as extending the integration time, increasing the excitation power or enhancing the brightness of signal source (fluorescent probe). The absorption of water was mainly considered in our study because water is the most abundant component in living organisms. The absorption spectrum of water in the band of 700–2300 nm is shown in Fig. 1b. The figure illustrates two major absorption peaks at ~1450 and ~1930 nm. Theoretically, the imaging quality could be improved in the spectral region around the peaks if the signal intensity is sufficient to overcome the attenuation due to absorption. This idea has been supported by recent studies those have discovered the advantages of *in vivo* imaging in 1400–1500 nm band^{13,20}. Bioimaging studies were absent in the vicinity of 1930 nm because the huge water absorption peak at ~1930 nm was regarded as an insurmountable barrier. In fact, the light absorption of water in the narrow spectral region around the peak is relatively low, which may not be insurmountable. Similar to NIR-IIx window, there is an opportunity for high-quality bioimaging in 1880–2080 nm as long as the fluorescent probe is bright enough to overcome the attenuation from water absorption. Under this perspective, 1880 nm may no longer be the boundary of the NIR-II region. Furthermore, with better scattering suppression at longer wavelengths, coupled with the positive effect of water absorption, the 1880–2080 nm window theoretically offers superior imaging quality to other NIR-II band regions.

To verify the above hypotheses, Monte Carlo method was employed to simulate photon propagation within 1200–1300 nm, 1300–1400 nm (NIR-IIa), 1400–1500 nm (NIR-IIx), 1500–1700 nm (NIR-IIb), 1700–1880 nm (NIR-IIc), and 1880–2080 nm windows (see Fig. 1c) in biological tissues. The line source set up for the simulation is shown in Supplementary Fig. S1. The SBR and structure similarity index measure (SSIM) of the simulated images within each band are shown in Fig. 1d, e. The images in NIR-IIx and 1880–2080 nm showed higher SBR and SSIM compared with those in other regions. It can be learned that enhanced absorption combined with reduced scattering contribute positively to more accurate imaging, for the main reason that higher absorption consumes more multiple scattered photons. Note that the background interference of image in 1880–2080 nm was particularly weak, attributed to the wavelength redshift and unique water absorption. Therefore, the 1880–2080 nm window showed great imaging potential, based on theoretical analysis and simulation results. With the rapid development of near-infrared sensitive detectors, as well as fluorescent probes with long-wavelength emission and high brightness, it is no longer impossible to realize *in vivo* fluorescence imaging in 1880–2080 nm as in simulations.

High-contrast *in vivo* imaging around the high absorption peak at ~1930 nm

In this section, experiments were conducted for *in vivo* fluorescence imaging in the 1880–2080 nm band. A series of PbS/CdS core-shell QDs were used as fluorescent probes, whose bright emission was

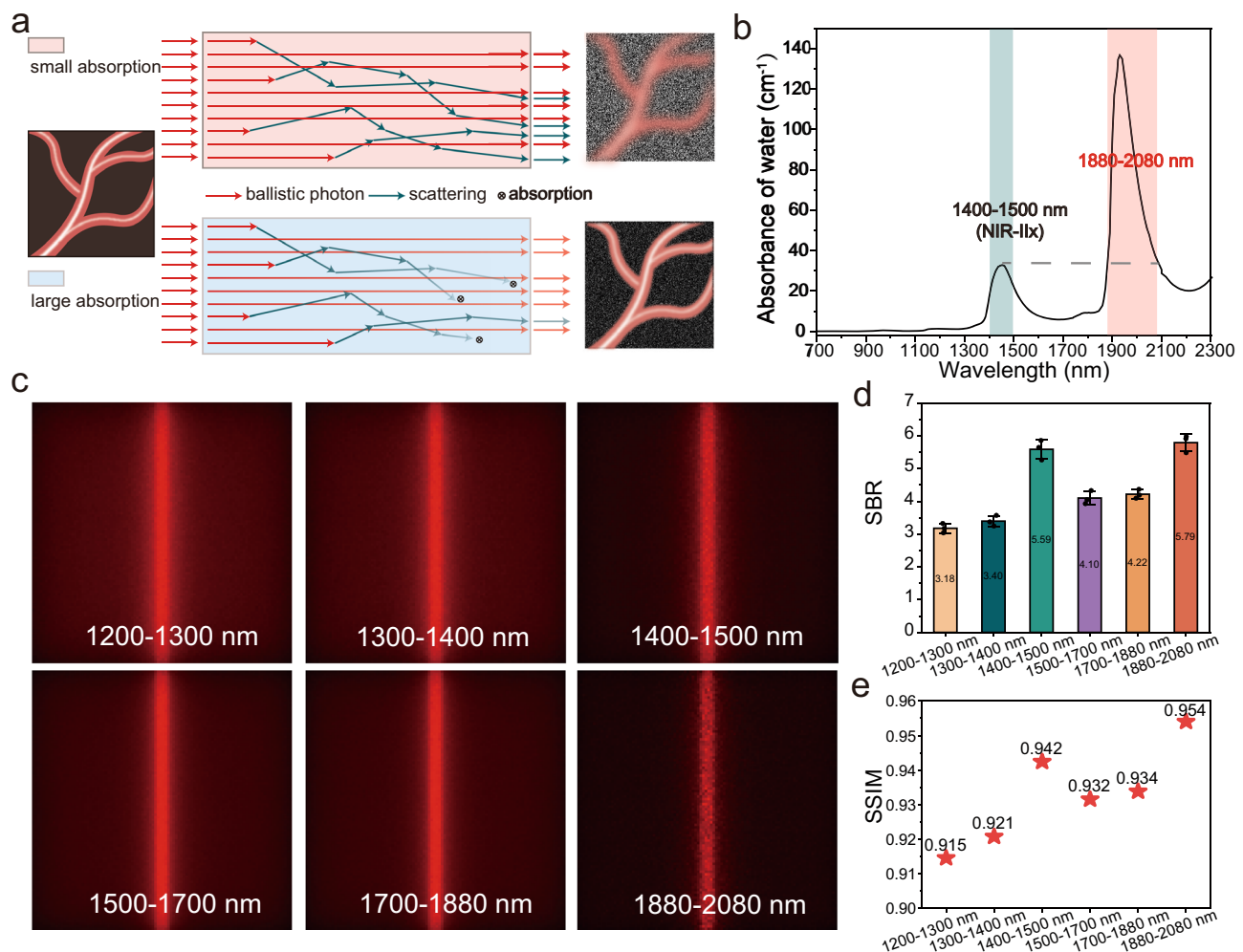


Fig. 1 | The schematic diagram of photon propagation in tissue and the simulation results of bioimaging via the Monte Carlo method. a Schematic of photon propagation in biological tissues with high and low light absorption, and the corresponding imaging effects. **b** The absorption spectrum of water within 700–2300 nm²⁷. **c** Simulated images within 1200–1300, 1300–1400, 1400–1500, 1500–1700, 1700–1880, and 1880–2080 nm, through routine biological tissue of

1 mm thickness, where the absorption coefficient of water was considered as the tissue absorption coefficient and the setting of tissue scattering coefficient could be found in the “Methods” section. **d** SBR analysis of the simulation results. $n = 3$ positions were randomly selected for analysis, data are presented as mean \pm SD. **e** The structure similarity index measure (SSIM) analysis of the simulation results.

expected to overcome the effects of water absorption during imaging. PbS/CdS QDs were synthesized based on our previous work²⁴ and were hydrated with polyethylene glycol (PEG) (Fig. 2a). Its cadmium sulfide (CdS) shell could protect the lead sulfide (PbS) core from oxidation and retain its bright fluorescence. Four types of PEGylated PbS/CdS QDs with different emission peak wavelengths were employed to objectively evaluate the fluorescence imaging within each NIR window. These QDs were named as 1100QD, 1300QD, 1450QD and 1700QD here in ascending order of emission wavelength. Their emission spectra in water are shown in Fig. 2b, and absorption spectra are shown in Fig. S2. Transmission electron microscopic (TEM) images (Fig. S3a) and dynamic light scattering (DLS) results (Fig. S3b) illustrate that the PbS/CdS QDs were spherically homogeneous and the average hydrodynamic sizes of PEGylated PbS/CdS QDs were all less than 45 nm. The four kinds of PEGylated PbS/CdS QDs were mixed in a specific ratio to obtain hybrid QDs fluorescent probes with bright emission covering all bands. The normalized absorption and emission spectra are shown in Fig. 2c. In addition, due to the broad-spectrum absorption of the QDs, the 1064 nm laser excitation, which has larger maximum power exposure (MPE) value for biological tissues, can be used. Thereby, higher excitation intensities are allowed, which can compensate to some extent for the attenuation of the signal caused by absorption.

The hybrid QD fluorescent probes (200 μ L) was intravenously injected into mice, and their blood vessels in legs were imaged within 1200–1300, 1300–1400, 1400–1500, 1500–1700, 1700–1880 and 1880–2080 nm bands, under the excitation of a 1064 nm CW laser (Fig. 2d–i). The results indicate a significant reduction in image background in the 1400–1500 and 1880–2080 nm windows (Fig. 2j), which have larger water absorption. The quantitative results in Fig. 2k also demonstrated that imaging in the 1400–1500 and 1880–2080 nm windows provided better SBRs of 2.77 and 2.91, respectively, compared with those in other windows. Note that the imaging performance of the 1400–1500 nm band was superior to that of 1500–1700 and 1700–1880 nm bands, for the reason that water absorption around 1450 nm had a significant positive effect, even surpassing the impact of scattering reduction caused by wavelength redshift. In contrast, the 1880–2080 nm window has the largest water absorption and lowest scattering among all these NIR sub-windows. Moreover, compared to the huge absorption peak at 1930 nm, the water absorption in the region slightly away from the peak is relatively low and can be overcome. Indeed, bioimaging in the 1880–2080 nm window has demonstrated its high contrast advantage (Fig. 2i). Thus, it is concluded that, redshifting

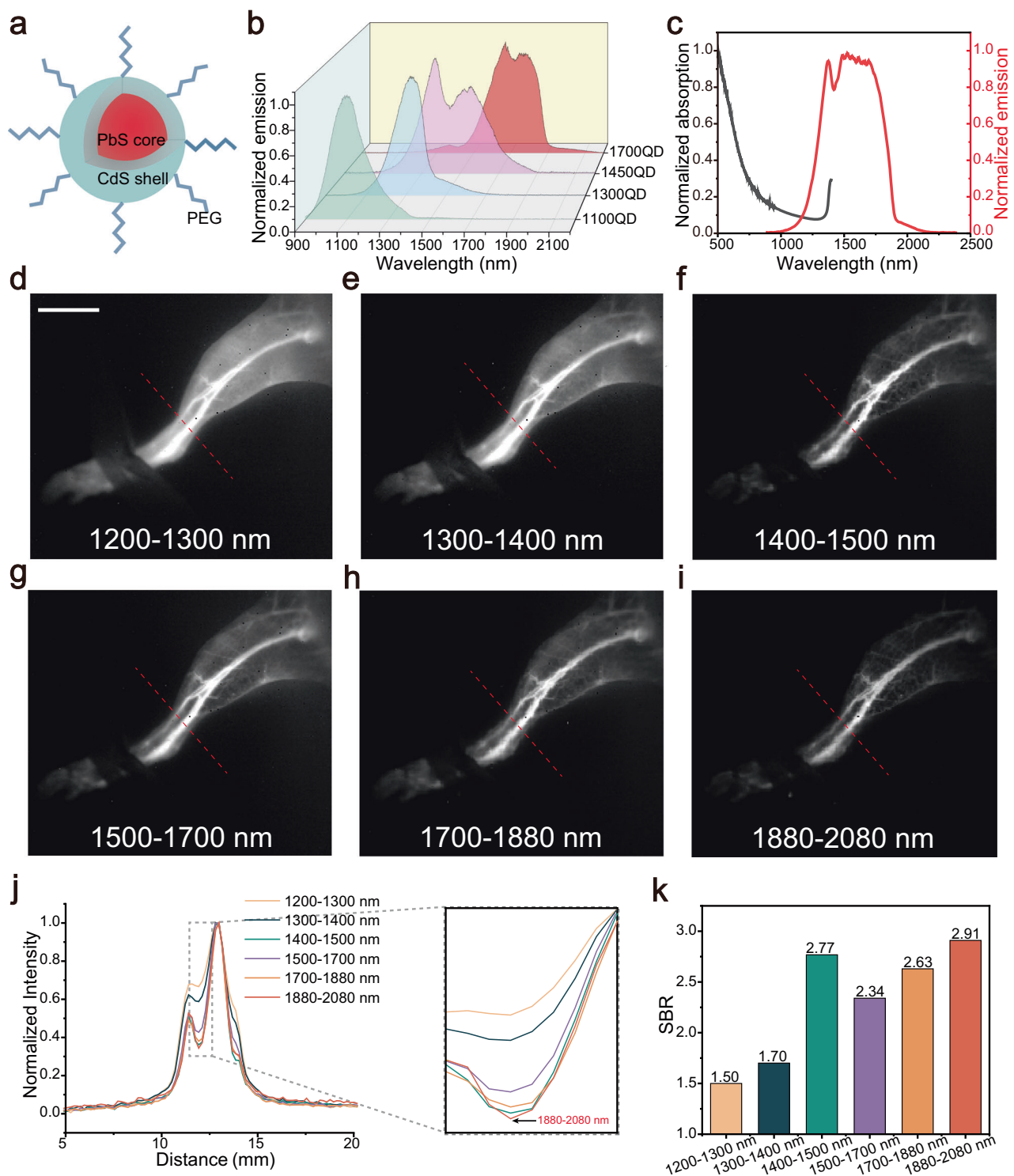


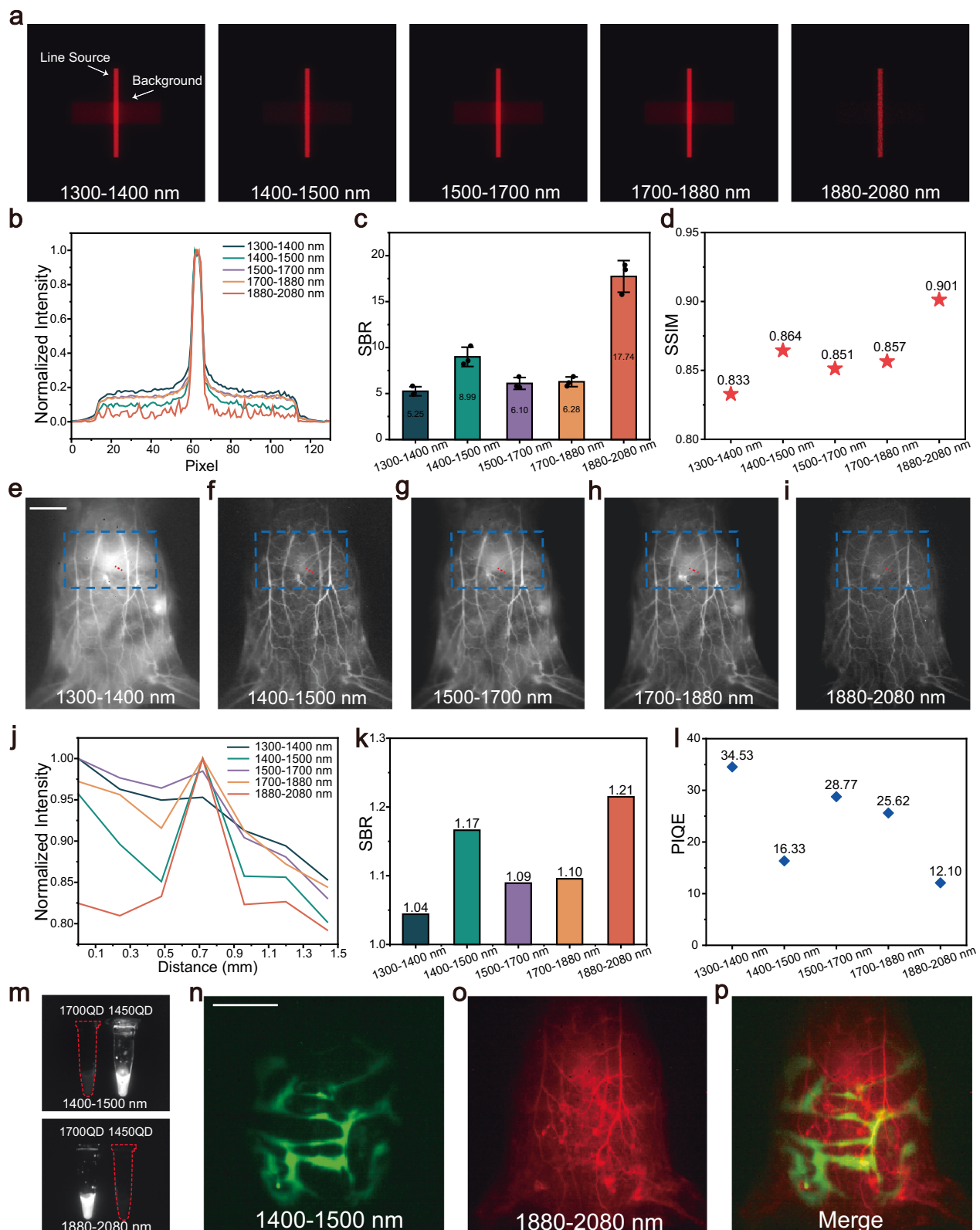
Fig. 2 | Comparison of in vivo fluorescence imaging of mice within various NIR bands. a Schematic design of the PEGylated PbS/CdS core-shell QDs. **b** Normalized emission spectra of four kinds of PEGylated QDs in aqueous dispersion. **c** Normalized absorption and emission spectra of four kinds of PEGylated QDs mixed in a certain ratio in water. The hind limb fluorescence images of the

same mouse in **d** 1200–1300 nm, **e** 1300–1400 nm, **f** 1400–1500 nm, **g** 1500–1700 nm, **h** 1700–1880 nm, and **i** 1880–2080 nm. Scale bars: 10 mm. **j** Cross-sectional fluorescence intensity profiles along the red dashed lines of the vessel in (d–i) and the localized magnification of the background signal. **k** SBR analysis of the imaging results in (d–i).

the window to 1880–2080 nm could significantly suppress the background (Fig. 2j), providing imaging performance even better than NIR-IIx window.

Many fluorescent dyes are excreted from the body through hepatic and renal metabolism, and these organs are also where they

accumulate²⁸. For example, ICG, a near-infrared fluorescent dye approved by the Food and Drug Administration, rapidly accumulates in organs like the liver after entering the bloodstream²⁹. The dye accumulating in the liver and spleen would create a bright background, and interfere with the detection of targeted vessels above



the organs. Simulations and in vivo experiments are conducted to explore the fluorescence imaging effects in these conditions. Figure 3a shows the simulation results by Monte Carlo method. The rectangular area (depth = 1.3 mm) below the orthogonal line source (depth = 1 mm) acted as the background, which was designed to simulate the imaging scene with strong background interference from deeper places. Due to water absorption around the -1450 and

-1930 nm peaks, original strong background located deeper was highly attenuated. Therefore, interference from deep non-targets was greatly reduced for imaging in the 1400–1500 and 1880–2080 nm windows, as demonstrated by the quantitative analysis (Fig. 3b). As a result, imaging in 1400–1500 and 1880–2080 nm provided the better SBR of 8.99 and 17.74, respectively (Fig. 3c). SSIM further demonstrated the superiority of the 1880–2080 nm window,

Fig. 3 | Comparison of in vivo NIR-II fluorescence imaging upon a bright background and multi-channel imaging of mice. **a** Simulated images in 1300–1400, 1400–1500, 1500–1700, 1700–1880 and 1880–2080 nm of the line source above a rectangular background (depth = 1.3 mm) through a routine biological tissue of 1 mm thickness, where the absorption coefficient of water was considered as the tissue absorption coefficient and the setting of tissue scattering coefficient could be found in the “Methods” section. **b** Fluorescence intensity profiles on the cross-section of the simulated samples above the rectangular backgrounds. **c** SBR analysis of the simulation results in **(a)**. $n = 3$ positions were randomly selected for analysis, data are presented as mean \pm SD. **d** SSIM analysis of the simulation results in **(a)**. Whole-body fluorescence imaging of the same mouse

in **e** 1300–1400 nm, **f** 1400–1500 nm, **g** 1500–1700 nm, **h** 1700–1880 nm and **i** 1880–2080 nm bands. Scale bars: 10 mm. **j** Cross-sectional fluorescence intensity profiles along the red dashed lines of the blood vessels in **(e–i)**. **k** SBR analysis of the imaging results in **(e–i)**. **l** The perception-based image quality evaluator (PIQE) analysis of the liver areas highlighted by the blue boxes in **(e–i)**. **m** Fluorescence images of the centrifuge tubes containing 1450QD and 1700QD in 1400–1500 and 1880–2080 nm bands. **n–p** In vivo dual-channel fluorescence imaging of mice. **n** An abdominal image of mouse intraperitoneally injected with 1450QD. **o** A vascular image of mouse intravenously injected with 1700QD. **p** The merged image of **(n, o)**. Scale bars: 10 mm.

as it was the only one exceeding 0.9 (Fig. 3d). In short, the 1880–2080 nm window has a more pronounced suppression of the strong background due to larger water absorption.

To directly compare and assess the quality of in vivo imaging in different imaging windows, the hybrid QDs fluorescent probes (200 μ L) were injected intravenously into a mouse for the whole-body vascular imaging (Fig. 3e–i). Ten minutes after injection, QDs accumulated in organs such as the liver and spleen, creating bright background areas. Thus, it became difficult to accurately observe the vessels above these bright organs. In the commonly used NIR-II sub-windows (NIR-IIa, NIR-IIb and NIR-IIc), fluorescence signals of the tiny blood vessels above the liver were almost submerged in the background and hard to distinguish, as demonstrated in Fig. 3e, g, h. While in the NIR-IIx and 1880–2080 nm windows, water absorption suppressed the background from the deeper area, because of the distinct attenuation of signals from the deeper organs through longer optical paths. Indeed, by analyzing the intensity profiles along the red dashed lines (positions shown in Fig. 3e–i), Fig. 3j demonstrated the lower background of fluorescence images in these two windows. Thus, fine vascular signals above the liver could be identified in NIR-IIx and 1880–2080 nm windows (Fig. 3f, i) with increased water absorption. The quantitative results of SBR and Perception-based Image Quality Evaluator (PIQE) demonstrated the same conclusion (Fig. 3k, l). Among them, the image in 1880–2080 nm window shows the best SBR of 1.21 and PIQE of 12.10, and that in the NIR-IIx window shows the second-best SBR of 1.17 and PIQE of 16.33. Overall, in cases with the inference of strong deep background, large water absorption significantly improves imaging quality by suppressing the background caused by the multiple scattered signal photons. Thus, the 1880–2080 nm window demonstrates an advantage in imaging contrast and is suitable for visualizing shallow targets above a strong background.

Taking advantage of the high imaging contrast at 1400–1500 and 1880–2080 nm bands, we achieved high-quality dual-channel imaging based on these two windows. Figure 3m shows the images of centrifuge tubes containing 1450QD and 1700QD respectively in the 1400–1500 and 1880–2080 nm windows, under CW laser excitation of 1064 nm. Quantitative analysis (Fig. S4) shows that the signal crosstalk between the 1400–1500 and 1880–2080 nm windows was negligible, which is important for multi-channel imaging. To further demonstrate the application of dual-channel imaging based on these two high-quality windows, we implemented in vivo fluorescence imaging on mice. 1450QD was injected intraperitoneally into mice for abdominal imaging, and 1700QD was injected intravenously for whole-body vascular images. Clear and discernible results were obtained in both 1400–1500 and 1880–2080 nm windows (Fig. 3n, o), and Fig. 3p shows the accurate merged image generated by software (Image J). In this case, the previously unexplored 1880–2080 nm band showed its advantage of high contrast in bioimaging, providing an imaging window option for multi-channel imaging. It is believed that this discovery can provide an important reference for future applications of the NIR band, especially for high-quality in vivo fluorescence imaging.

Simulation and exploration of near-infrared fluorescence bioimaging windows in adipose tissue

The human body is mainly composed of water, proteins, fats, and inorganic substances. Tissues with various compositions have different light absorption and photon scattering properties, thus different effects on optical imaging. Most of the previous studies have been based on water absorption, considering that water accounts for the most in living organisms. However, conclusions drawn in such particular imaging models are unlikely to be fully applicable to different tissue environments. In fact, a major component of the human body is body fat, accounting for about 20%, second only to water and protein, and the percentage of fat in obese people can even be as high as 40%^{30,31}. In recent years, studies have begun to focus on adipose as a tissue component in hyperspectral imaging³¹. However, there is a paucity of studies targeting the well-developed theory of imaging windows in adipose tissue, especially at the long wavelength window. Therefore, the exploration of adipose tissue has significant clinical value. Here, we conducted a series of experiments to explore the effect of adipose tissue on imaging and the optimal imaging window for adipose tissue.

To mitigate the research gap, we tested the optical parameters of absorption and reduced scattering of porcine adipose tissue (Fig. 4a, b). There are two similar absorption peaks within the 1700–1880 and 1880–2080 nm windows in the adipose tissue. According to the theory, 1700–1880 and 1880–2080 nm windows with low photon scattering and appropriately increased light absorption have good imaging potential for adipose tissue. Based on the tested absorption and reduced scattering spectra of adipose tissue, fluorescence imaging through adipose tissue of different thicknesses within different spectral bands was simulated by Monte Carlo method. Note that the 1700–1880 and 1880–2080 nm windows have similar absorption and scattering properties, and the simulation results and corresponding quantitative analysis also give evidence that these two windows had similar imaging quality (Fig. S5). It indicates that 1700–2080 nm could be used as an entire window which has high contrast imaging potential for adipose tissue imaging. Therefore, 1700–2080 nm was considered as an integrated window in the following studies. Figure 4c shows the simulated imaging results within 900–1100, 1100–1300, 1300–1400, 1400–1500, 1500–1700, and 1700–2080 nm windows, through 1, 2 and 3 mm thicknesses of adipose tissue respectively. Simulated image results in the 600–900 nm band are shown in Fig. S6. The contrast of the simulation results in the 1700–2080 nm window was obviously much higher than those in other windows. SBR and SSIM analyses also give evidence to support the conclusion (Fig. 4d, e). The overall trend was that image quality improved with wavelength increasing, except for the 1400–1500 nm window, which had a relatively better SBR and SSIM compared to 1500–1700 nm due to its higher absorption in the adipose tissue. This further confirmed the positive effect of appropriately increased absorption on imaging. Overall, the 1700–2080 nm window with unique light absorption and reduced photon scattering provides the best imaging performance in adipose tissue. This conclusion provides

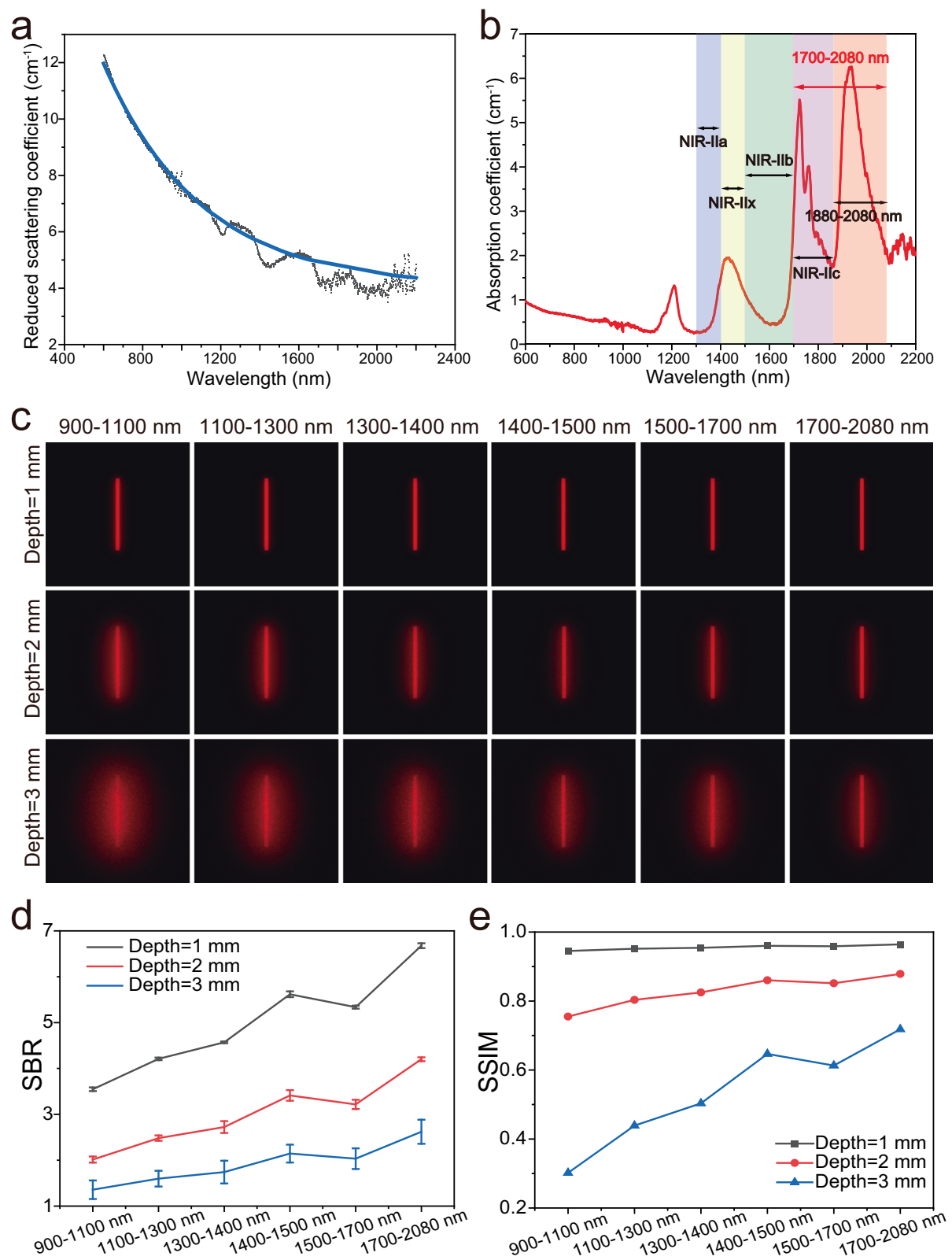


Fig. 4 | The simulation results of NIR fluorescence imaging through adipose tissue via the Monte Carlo method. a Reduced scattering spectra of adipose tissue within 600–2200 nm and its fitted curve. **b** Absorption spectra of adipose tissue within 600–2200 nm. **c** Simulated fluorescence images of a line source passing through the adipose tissue of 1, 2 and 3 mm thicknesses within the

900–1100, 1100–1300, 1300–1400, 1400–1500, 1500–1700, and 1700–2080 nm windows. **d** SBR analysis of the simulation results at different depths. $n = 3$ positions were randomly selected for analysis, data are presented as mean \pm SD. **e** SSIM analysis of the simulation results at different depths.

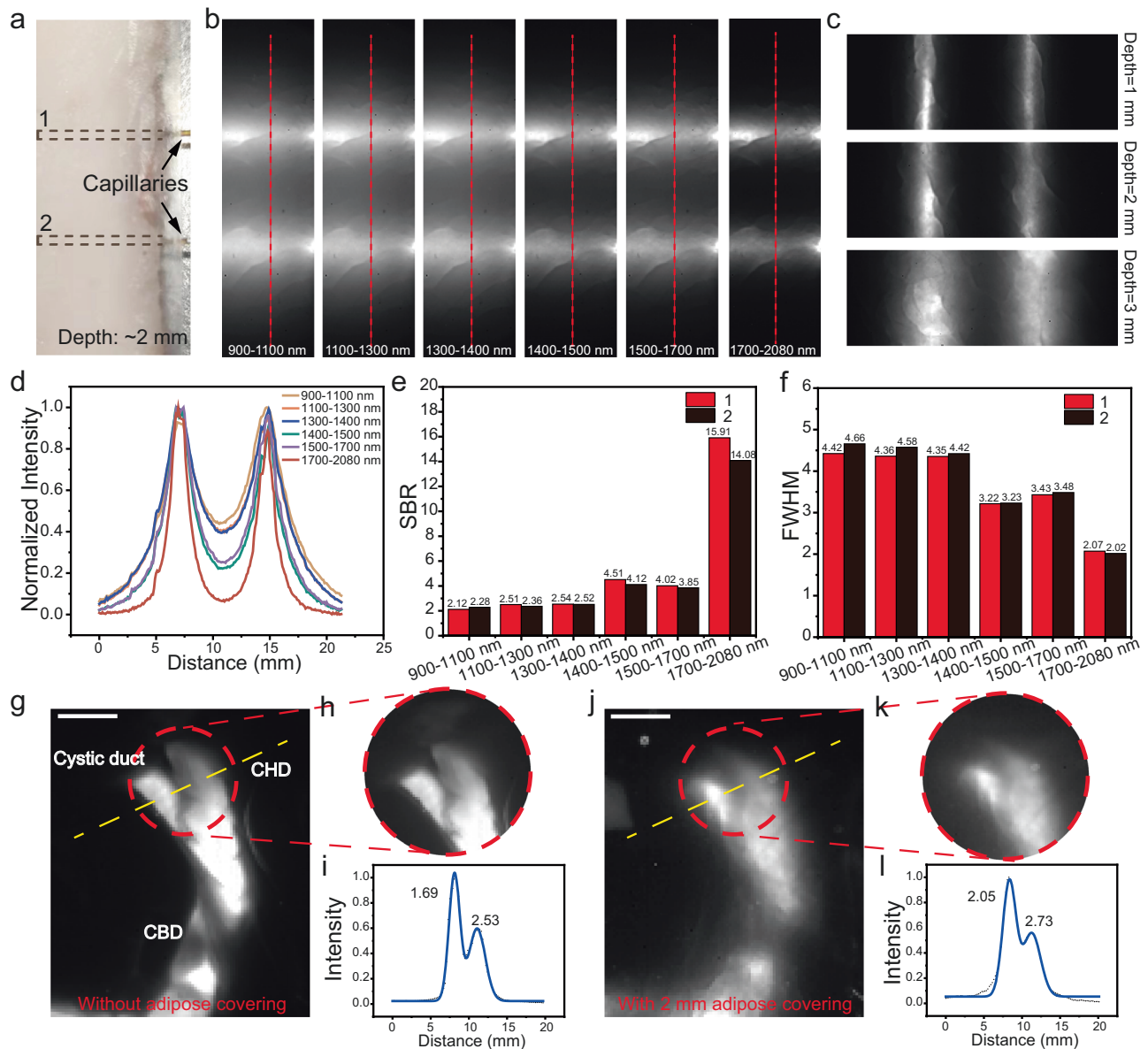


Fig. 5 | In vitro and in vivo experiments for NIR fluorescence imaging through adipose tissue. **a** A bright-field image showing two capillaries loaded with hybrid QDs fluorescent probes and buried in the porcine adipose tissue. **b** Fluorescence images of capillaries through adipose tissue of 2 mm thickness within 900–1100, 1100–1300, 1300–1400, 1400–1500, 1500–1700, and 1700–2080 nm windows. **c** Fluorescence images of capillaries through adipose tissue of 1, 2, and 3 mm thickness at the 1700–2080 nm window. **d** Normalized fluorescence intensity profiles along the red dashed lines in **(b)**. **e** SBR analysis of the profiles in **(d)**. **f** FWHM analysis of the profiles in **(d)**. **g, h** Fluorescence images of rabbit bile ducts

without adipose tissue covered in the 1700–2080 nm window. Scale bars of **(g)**: 5 mm. CHD common hepatic duct, CBD common bile duct. **i** Normalized fluorescence intensity profile along the yellow dashed line in **(g)** and the corresponding Gaussian-fitted FWHM value. **j, k** Fluorescence images of rabbit bile ducts covered with porcine adipose tissue of ~2 mm thickness in the 1700–2080 nm window. Scale bars of **(j)**: 5 mm. **l** Normalized fluorescence intensity profile along the yellow dashed line in **(j)** and the corresponding Gaussian-fitted FWHM value, where the dots represent the raw data and the blue line represents Gaussian fitted curves.

valuable insights for the selection of fluorescence imaging windows in clinical applications, especially in adipose-rich environments.

This conclusion is supported by the actual imaging results. In the experiments, two parallel capillaries filled with the hybrid QDs fluorescent probes were inserted horizontally into the porcine adipose tissue (capillaries buried at a depth of 2 mm, see Fig. 5a). Fluorescence imaging of the capillaries within the 900–1100, 1100–1300, 1300–1400, 1400–1500, 1500–1700, and 1700–2080 nm windows was performed under the excitation of a 793 nm CW laser (Fig. 5b). To further evaluate the effectiveness and penetration ability of the 1700–2080 nm window for imaging in adipose tissue,

fluorescence images of the capillaries at different depths were also taken. Figure S7 shows images of capillaries buried at depths of 1, 2, and 3 mm within different windows. The fluorescence images obtained at 1700–2080 nm band were precise and clear, even at a depth of 3 mm (Fig. 5c). Figure 5d shows the fluorescence intensity profiles along the red dashed line in Fig. 5b. The background between these two capillaries was lowest in the 1700–2080 nm window due to the unique absorption and low scattering, with the 1400–1500 nm window ranked second because of its somewhat absorption. Quantitative analysis of the imaging results (Fig. 5e, f) also shows that both increased absorption and reduced scattering contribute to precise

imaging. Image in the 1700–2080 nm window had the best SBR and full width at half maximum (FWHM), which was in agreement with the theory and simulation results. To summarize, the *in vitro* experimental results strongly prove that the 1700–2080 nm window proposed in this paper has the best imaging performance in adipose tissue.

The imaging advantages of the 1700–2080 nm window in adipose tissue still exist for *in vivo* imaging applications. Morbid obesity is generally considered a risk factor for laparoscopic cholecystectomy because of increased operative time, morbidity, and conversion to open cholecystectomy^{32,33}. The anatomical surface of the gallbladder triangle often becomes complex due to fat accumulation, inflammation, adhesions, and other factors³⁴. This would pose a challenge for accurate identification of extrahepatic bile ducts during laparoscopic cholecystectomy (LC) in these patients, which can be greatly assisted by fluorescent cholangiography at present^{35–39}. Therefore, it is quite important to visualize the deep structures buried in the adipose tissue. In the following *in vivo* experiment, fresh porcine fat is employed to cover the rabbit bile ducts to simulate fat accumulation and tissue thickening. Biliary fluorescence imaging in the 1700–2080 nm window was performed after the hybrid QDs fluorescent probes were injected retrogradely into the rabbit common bile duct. In the absence of adipose coverage, biliary structures including the cystic duct, common hepatic duct (CHD), and common bile duct (CBD) were illuminated, and the fluorescence images showed high resolution and remarkably low background signal in the 1700–2080 nm window (Fig. 5g). This was also consistent with the biliary structures shown in the bright-field image (Fig. S8). On this basis, ~2 mm thick fresh porcine adipose tissue was placed to cover the biliary region to simulate fat accumulation. Even under the influence of adipose tissue, accurate visualization of biliary structures still could be realized in the 1700–2080 nm window, as shown in Fig. 5j. The biliary tract structures were clearly delineated and consistent with the image that was not covered by the adipose tissue. In the simulated complex environment of a gallbladder triangle with fat adhesions and tissue thickening, the junction of the cystic duct and CHD remained distinctly visible in the 1700–2080 nm window with high contrast. This imaging capability can serve as a positive guidance for identifying safe transection locations on the cystic duct during the cholecystectomy. In contrast, it was difficult for fluorescence imaging in 900–1700 nm (Fig. S9) to clearly distinguish the genera-branching structures of bile ducts, which could be discriminated in the fluorescence image in the 1700–2080 nm window (Fig. 5j) and the bright field image (Fig. S8). The 1700–2080 nm window, with low scattering and increased absorption in adipose tissue, shows its imaging advantages in penetration depth and spatial resolution, which are critical for accurately identifying deep biliary structures obscured by adipose tissue. These results prove that it is meaningful to consider the effects of absorption and scattering of various tissues on imaging in complex biological environments. In conclusion, *in vivo* fluorescence imaging in 1700–2080 nm window exhibits significant superiority in adipose tissue due to the combined effect of absorption and scattering. We believe that this fluorescence imaging window holds great translational potential for diverse clinical applications in the foreseeable future.

Discussion

Achieving high-contrast, deep-tissue imaging has long been a challenge. The development of NIR-II fluorescence imaging offers significant potential for capturing details *in vivo* with high contrast. The selection of imaging windows based on scattering and absorption principles is crucial for the development of fluorescence imaging, especially for biomedical applications. In past studies, regions with large water absorption were considered unsuitable for imaging because of signal attenuation. However, with the development of bright fluorophores and growing exploration of the positive effects of

absorption, the region beyond 1880 nm is no longer a forbidden zone for NIR imaging. Our simulation results showed that 1880–2080 nm imaging exhibited high contrast when the photon count was sufficient to overcome the absorption-related attenuation. Although only the emission trailing of the off-peak fluorescent probe was utilized in the experiments, the 1880–2080 nm window demonstrated an excellent imaging quality, comparable to NIR-IIx, which has been recognized as a promising sub-window with high contrast in the NIR-II region. These findings suggest that the 1880–2080 nm region is an optimal choice for high-quality fluorescence imaging when the attenuation effects of absorption are properly overcome. This discovery, based on a deep understanding and utilization of the positive role of tissue absorption, breaks the boundary of previously held limitation of NIR-II imaging. Attributed to the fact that absorption can better suppress background signals from the depths, the 1880–2080 nm window enables visualization of shallow targets with high contrast under strong background interference. Furthermore, the 1880–2080 nm window also provides a viable option for multi-channel fluorescence imaging applications.

It is important to note that absorption will inevitably cause attenuation of signal intensity when imaging in windows with large absorption. However, the loss can be mitigated through several strategies, such as selecting brighter fluorescent probes, increasing the intensity of excitation, or extending detection time. In this study, we chose an off-peak QDs fluorescent probe as an effective compromise. The probe exhibited strong fluorescence intensity, sufficient to overcome the absorption attenuation. As a result, we successfully demonstrated the feasibility and superiority of imaging in the 1880–2080 nm region. These findings provide valuable insights for off-peak fluorescence bioimaging and may further promote the development of NIR-II fluorescent probes. We also anticipate that high-brightness fluorescent probes with more compatible long-wavelength emission can be exploited in the future.

The aim of this study is to identify superior and suitable imaging windows for complex biological environments, utilizing the imaging contrast enhancement due to tissue absorption. Most recent studies have primarily focused on the absorption of water, the most abundant component of biological tissues. In contrast, our research has expanded the scope to include adipose tissue, another major constituent of living organisms. Through simulations, *in vitro* experiments and *in vivo* experiments, we have demonstrated that the 1700–2080 nm region with moderate absorption and low scattering has optimized imaging quality in adipose tissue. This conclusion offers a more accurate and tissue-specific perspective compared to findings based solely on water absorption. In addition, we conducted additional simulation involving both skin and adipose tissue to demonstrate the effectiveness of this window in a broader range of clinically relevant applications (Fig. S10). In recent years, NIR-II fluorescence imaging has achieved remarkable success in guiding clinical surgery. However, it remains uncertain whether similar optimal imaging results can be obtained in specific tissues with different absorption and scattering parameters. The selection of optimal imaging windows based on scattering and absorption principles will depend on specific tissue environments, which requires more meticulous exploration and research. Our results of the exploration and validation of imaging in adipose tissue also support this understanding. These findings are expected to promote further development and application of NIR-II fluorescence imaging. Additionally, beyond fluorescence imaging, the interaction between light and biological tissues should be re-evaluated in the context of other advanced imaging techniques, such as the effect of absorption on the contrast of hyperspectral imaging⁴⁰, despite the inherent physical differences between these methods. We look forward to conducting more comprehensive research and assessment of how absorption and scattering influence different imaging technologies, thereby promoting technological integration and application expansion.

Methods

The simulation of photon propagation in biological tissues via Monte Carlo method

The fluorescent signal source is set as a line of 2 mm long and 0.1 mm wide, and emits a total of 1×10^7 photons in random directions. The refractive index of tissues is set as 1.37 and the scattering anisotropy factor is set as 0.9. The dimensions of the tissue in the simulation are set as 100 mm in both length and width. After the photon has propagated through the tissue, it travels through the macroscopic imaging system and reaches the detector. The detector is a 2D array plane with a resolution of 512×512 and the pixel size is set to 20 μm . In simulations of vascular imaging in routine tissues, the absorption coefficient of water is assumed to be the absorption coefficient of the tissue, considering that water is the most predominant component of biological tissues. The scattering coefficient adopts an empirical value¹³. In the first vascular imaging simulation, the line source is set at a depth of 1 mm and extended background from different depths are added to simulate background such as tissue autofluorescence. For the simulation of a vascular imaging scene under strong background interference at depth, in addition to a vertical line light source (depth = 1 mm), a horizontal line source (depth = 1.3 mm) with a length of 2 mm and a width of 0.5 mm which emits a total of 5×10^7 photons in random directions is set up to act as the strong background caused by the liver. In the simulation of imaging in adipose tissue, the previously measured absorption and reduced scattering spectra of fresh porcine adipose by the integrating sphere method are used for the simulation. The specific measurement steps are described in the supporting information. On this basis, separate simulations are performed for vertical line source buried at tissue depths of 1, 2, and 3 mm.

Optical system for fluorescence imaging

The self-constructed NIR-II fluorescence macro imaging system includes an excitation light source and an imaging module. Two CW lasers of 793 and 1064 nm are used as excitation sources, in which 793 nm excitation offers the advantage of higher excitation efficiency (Fig. S11) while 1064 nm excitation provides the benefit of a higher safe power density limit. After being collimated, the laser beam is expanded through a lens and then further homogenized by a ground glass diffuser, ensuring that a uniform illumination is produced on the observing sample. The fluorescence emitted from the sample passes through the filters and objective lens, and then is imaged on the detector of a customized HgCdTe camera (spectral range of 900–2500 nm). According to the SDK of the camera's standard interface communication protocol, an independent software has been customized (with the function of loading, collecting and saving images). The objective lens used is OLES30 (SPECIM, Finland, focal length = 30.7 mm, transmission spectral range of 850–2500 nm). In all our experiments, we readjust the objective lens for imaging in different wavebands to achieve correct focusing, ensuring that image clarity is maintained across the entire NIR spectral range (Fig. S12). Imaging in different windows of the research is achieved by using a variety of long-pass (LP) and short-pass (SP) filters detailed in Supplementary Table 1. In the *in vivo* fluorescence imaging experiments, the highest excitation intensity used is 0.16 W/cm² for the 793 nm CW laser and 0.4 W/cm² for the 1064 nm CW laser, which are both below the laser safety limits for NIR lasers (U.S. National Standard for Safe Use of Lasers, ANSI Z136.1-2014). The highest excitation intensity used is 0.29 W/cm² for the 793 nm CW laser in the *in vitro* fluorescence imaging experiments. The integration times for imaging are all 70 ms.

Chemicals

PbCl₂, CdO, and sulfur powder were purchased from Alfa. Oleylamine, oleic acid, 1-octadecene (ODE), poly(acrylic acid) (MW ~1800), 2-(*N*-morpholino)ethanesulfonic acid (MES), *N*, *N*'-dicyclohexylcarbodiimide (DCC), *N*-(3-dimethylaminopropyl)-*N*'-ethylcarbodiimide hydrochloride

(EDC), were purchased from SigmaAldrich. mPEG-amine (MW ~5 K) was purchased from Laysan Bio. 8-Arm PEG-amine (MW ~40K) was purchased from Advanced BioChemicals.

Synthesis of PbS/CdS QDs

The sulfur precursor solution was prepared by mixing 0.08 g of sulfur powder with 7.5 mL of oleylamine in a two-neck flask under argon at 120 °C for 30 min. The lead precursor solution was prepared by combining 0.834 g of PbCl₂ and 7.5 mL of oleylamine in a three-neck flask, degassing under argon for 30 min, and then heating to 45–160 °C (depending on the desired particle size). Under continuous stirring, 2.25 mL of the sulfur precursor solution was injected into the lead precursor solution. Once the desired growth time (typically 3–90 min) was reached, the reaction was quenched by adding 10 mL of cold hexane. The products were collected via centrifugation and redispersed in a mixture of 10 mL hexane and 20 mL oleic acid. The mixture was agitated for 10 min to remove excess sulfur from the products. The QDs were then precipitated by centrifugation. This precipitation procedure was repeated three times until the supernatant became colorless. The QDs were redispersed in a mixture of toluene and ODE. The PbS/CdS QDs were synthesized via a cation-exchange procedure. CdO (0.6 g), oleic acid (4 mL), and ODE (15 mL) were heated to 200 °C, purged with argon, and then cooled to 100 °C. 5 mL of PbS QDs in toluene/ODE was bubbled with argon for 5 min and then injected into the Cd precursor. The reaction flask was quenched by stopping stirring and heating immediately after the growth reaction was carried out at 100 °C for 20–120 min. The PbS/CdS QDs were precipitated with ethanol and then redispersed in hexane.

Modification and PEGylation of QDs

0.9 g of poly(acrylic acid) powder (average MW ~1800) and 1.56 g of DCC were transferred into a round-bottom flask. The mixture was dissolved in 10 mL of DMF, and approximately 1.2 mL of oleylamine was added dropwise. The solution was stirred overnight. After the reaction, 50 mL of 0.5 M HCl was added to the mixture. The resulting precipitate was separated by centrifugation and redissolved in 3 mL of methanol. Subsequently, 20 mL of 1 M HCl was added to the solution, and the precipitate was again separated by centrifugation. This purification process was repeated at least five times. The final precipitate was dissolved in 5 mL of chloroform and washed with 10 mL of 1 M HCl. The organic phase was collected and dried over anhydrous Na₂SO₄. The chloroform was removed under vacuum, yielding oleylamine-branched poly(acrylic acid) (OPA). As-synthesized PbS/CdS QDs (5.0 mg) were dissolved in 2.0 mL of chloroform containing 15 mg of OPA. The mixture was stirred at room temperature for 30 min, and the solvent was removed under vacuum using a rotary evaporator. The residue was then dissolved in 50 mM Na₂CO₃ solution under sonication. The modified QDs were precipitated by ultracentrifugation at 75,000 rpm for 1 h. The purified product was dissolved in pH 8.5 MES buffer (0.01 M) and stored at 4 °C. 15 mg of mPEG-amine (MW ~5 kDa) and 5 mg of 8-Arm PEG-amine (MW ~40 kDa) were dissolved in 1 mL of MES buffer at a molar ratio of 24:1 and added to the QDs dispersion under stirring. Additionally, 10 mg of EDC was dissolved in 500 μL of MES buffer and added to the QDs dispersion. The mixture was stirred at room temperature overnight. The PEGylated QDs were purified using a 100 kDa filter and washed five times with 1 \times PBS to remove excess reactants. The final product was dissolved in 1 \times PBS and stored at 4 °C.

Animal handling

All experimental procedures were approved by the Animal Use and Care Committee of Zhejiang University (#ZJU20220283). The experimental animals involved in this research included Institute of Cancer Research (ICR) mice (~20 g) and rabbits (~2 kg), which were obtained from SLAC Laboratory Animal Co. Ltd. (Shanghai, China). All the

experimental mice were housed under standard conditions at the Experimental Animal Centre of Zhejiang University and were fed water and food with a normal 12 h light/dark cycle at a room temperature of 24 °C and 50.0 ± 5.0% humidity.

In vivo fluorescence imaging of mouse

ICR mice (6–8 weeks, female) were depilated 1 day in advance. In the imaging performance comparison at each spectral band, mice were injected with 200 µL of hybrid PEGylated PbS/CdS QDs dispersion via the tail vein with an insulin needle to label blood vessels. The hybrid dispersion comprised 0.12 µM 1100QD, 0.24 µM 1300QD, 1.31 µM 1450QD, and 2.91 µM 1700QD. In dual-channel imaging, 100 µL of 4.5 µM 1450QD was injected intraperitoneally into mice for abdomen imaging, and 150 µL of 5 µM 1700QD was injected intravenously into mice for vascular imaging. The NIR-II macro fluorescence imaging system and a 1064 nm CW laser were used. The excitation intensity was less than 300 mW/cm² for vascular imaging over the liver, less than 400 mW/cm² for leg vascular imaging, and less than 80 mW/cm² for dual-channel imaging. The integration times for imaging were all 70 ms.

In vivo cholangiography of rabbits in various windows

Rabbit bile ducts are chosen as the experimental model because rabbits are mammals and have larger bile ducts, whose structure more closely resembles that of humans. In vivo biliary imaging in rabbits was performed by retrograde injection of PEGylated PbS/CdS QDs. The distal portion of the common bile duct was carefully dissected from the surrounding tissue and perforated by using microsurgical scissors. Then, a carotid artery catheter with an inner diameter of 1 mm was carefully inserted into the common bile duct and secured. The 200 µL of hybrid PEGylated PbS/CdS QDs were prepared as mentioned above and diluted to 800 µL. The QDs were injected through the catheter into the bile ducts at a slow and constant rate to avoid the risk of causing high intra-biliary pressure. The amount injected was controlled according to actual needs. To assess the penetration capability of 1700–2080 nm imaging in adipose tissue environments, the biliary region was covered with 2 mm thick fresh porcine adipose tissue. The NIR-II macro fluorescence imaging system and a 793 nm CW laser were used. The excitation intensity was less than 160 mW/cm² and the integration times were 70 ms for imaging.

Reporting summary

Further information on research design is available in the Nature Portfolio Reporting Summary linked to this article.

Data availability

All data generated or analyzed during the study are included in the article, Supplementary Information, and Source data file. Source data are provided with this paper.

Code availability

All codes in this paper are available upon request to the authors.

References

- Nagaya, T., Nakamura, Y. A., Choyke, P. L. & Kobayashi, H. Fluorescence-guided surgery. *Front. Oncol.* **7**, 314 (2017).
- Welsher, K. et al. A route to brightly fluorescent carbon nanotubes for near-infrared imaging in mice. *Nat. Nanotechnol.* **4**, 773–780 (2009).
- Hong, G. et al. Through-skull fluorescence imaging of the brain in a new near-infrared window. *Nat. Photonics* **8**, 723–730 (2014).
- Wang, P. et al. NIR-II nanoprobes in-vivo assembly to improve image-guided surgery for metastatic ovarian cancer. *Nat. Commun.* **9**, 2898 (2018).
- Hu, Z. et al. First-in-human liver-tumour surgery guided by multi-spectral fluorescence imaging in the visible and near-infrared-I/II windows. *Nat. Biomed. Eng.* **4**, 259–271 (2020).
- Fan, X. et al. Nanoprobes-assisted multichannel NIR-II fluorescence imaging-guided resection and photothermal ablation of lymph nodes. *Adv. Sci.* **8**, 2003972 (2021).
- Liu, Y. et al. Highly twisted conformation thiopyrylium photosensitizers for in vivo near infrared-II imaging and rapid inactivation of coronavirus. *Angew. Chem. Int. Ed. Engl.* **62**, e202214875 (2023).
- Li, Y. et al. Small-molecule fluorophores for near-infrared IIb imaging and image-guided therapy of vascular diseases. *CCS Chem.* **4**, 3735–3750 (2022).
- Gao, J. et al. Near-infrared II fluorescence imaging and image-guided siRNA therapy of atherosclerosis. *J. Med. Chem.* **67**, 12428–12438 (2024).
- Lyu, S. et al. A NIR-II photoacoustic/NIR-IIa fluorescent probe for targeted imaging of glioma under NIR-II excitation. *J. Med. Chem.* **67**, 1861–1871 (2024).
- Cao, Q., Zhegalova, N. G., Wang, S. T., Akers, W. J. & Berezin, M. Multispectral imaging in the extended near-infrared window based on endogenous chromophores. *J. Biomed. Opt.* **18**, 101318–101318 (2013).
- Diao, S. et al. Fluorescence imaging in vivo at wavelengths beyond 1500 nm. *Angew. Chem. Int. Ed. Engl.* **127**, 14971–14975 (2015).
- Feng, Z. et al. Perfecting and extending the near-infrared imaging window. *Light Sci. Appl.* **10**, 197 (2021).
- Wang, F. et al. In vivo non-invasive confocal fluorescence imaging beyond 1,700 nm using superconducting nanowire single-photon detectors. *Nat. Nanotechnol.* **17**, 653–660 (2022).
- Smith, A. M., Mancini, M. C. & Nie, S. Second window for in vivo imaging. *Nat. Nanotechnol.* **4**, 710–711 (2009).
- Chen, Z. H. et al. An extended NIR-II superior imaging window from 1500 to 1900 nm for high-resolution in vivo multiplexed imaging based on lanthanide nanocrystals. *Angew. Chem. Int. Ed. Engl.* **135**, e202311883 (2023).
- Tanzid, M. et al. Absorption-induced image resolution enhancement in scattering media. *ACS Photonics* **3**, 1787–1793 (2016).
- Carr, J. A. et al. Absorption by water increases fluorescence image contrast of biological tissue in the shortwave infrared. *Proc. Natl. Acad. Sci. USA* **115**, 9080–9085 (2018).
- Wu, T., Wang, Y., Lin, H. & Qian, J. A pervasive approach for determining the optimal tissue windows for near-infrared fluorescence imaging. *Laser Photonics Rev.* **19**, 2400628 (2025).
- Feng, Z. et al. Engineered NIR-II fluorophores with ultralong-distance molecular packing for high-contrast deep lesion identification. *Nat. Commun.* **14**, 5017 (2023).
- Zhang, Y. et al. Controlled synthesis of Ag₂Te@Ag₂S core-shell quantum dots with enhanced and tunable fluorescence in the second near-infrared window. *Small* **16**, 2001003 (2020).
- Chang, Y. et al. Bright Tm³⁺-based downshifting luminescence nanoprobes operating around 1800 nm for NIR-IIb and c bioimaging. *Nat. Commun.* **14**, 1079 (2023).
- Li, Y. et al. Design of AlEgens for near-infrared IIb imaging through structural modulation at molecular and morphological levels. *Nat. Commun.* **11**, 1255 (2020).
- Zhang, M. et al. Bright quantum dots emitting at ~1,600 nm in the NIR-IIb window for deep tissue fluorescence imaging. *Proc. Natl. Acad. Sci. USA* **115**, 6590–6595 (2018).
- Bashkatov, A., Genina, E., Kochubey, V. & Tuchin, V. J. O. Optical properties of the subcutaneous adipose tissue in the spectral range 400–2500 nm. *Optics Spectrosc.* **99**, 836–842 (2005).
- Tsai, C. L., Chen, J. C. & Wang, W. J. Near-infrared absorption property of biological soft tissue constituents. *J. Med. Biol. Eng.* **21**, 7–14 (2001).

27. Kou, L., Labrie, D. & Chylek, P. Refractive indices of water and ice in the 0.65-to 2.5- μm spectral range. *Appl. Optics* **32**, 3531–3540 (1993).
28. Hong, G., Antaris, A. L. & Dai, H. Near-infrared fluorophores for biomedical imaging. *Nat. Biomed. Eng.* **1**, 0010 (2017).
29. Desmettre, T., Devoisselle, J. & Mordon, S. Fluorescence properties and metabolic features of indocyanine green (ICG) as related to angiography. *Surv. Ophthalmol.* **45**, 15–27 (2000).
30. Hernández, A. *Adipose Tissue: What Is It, Location, Function, and More* (Elsevier, 2023).
31. St-Onge, M. Are normal-weight Americans over-fat? *Obesity* **18**, 2067–2068 (2010).
32. Finucane, M. M. et al. National, regional, and global trends in body-mass index since 1980: systematic analysis of health examination surveys and epidemiological studies with 960 country-years and 9.1 million participants. *Lancet* **377**, 557–567 (2011).
33. Ammori, B. et al. Laparoscopic cholecystectomy in morbidly obese patients. *Surg. Endosc. Ultras.* **15**, 1336–1339 (2001).
34. Daskalaki, D. et al. Indocyanine green (ICG) fluorescent cholangiography during robotic cholecystectomy: results of 184 consecutive cases in a single institution. *Surg. Innov.* **21**, 615–621 (2014).
35. Kuwabara, J. et al. Usefulness of laparoscopic subtotal cholecystectomy with operative cholangiography for severe cholecystitis. *Surg. Today* **44**, 462–465 (2014).
36. Dip, F. D. et al. Cost analysis and effectiveness comparing the routine use of intraoperative fluorescent cholangiography with fluoroscopic cholangiogram in patients undergoing laparoscopic cholecystectomy. *Surg. Endosc.* **28**, 1838–1843 (2014).
37. Larsen, S. S., Schulze, S. & Bisgaard, T. Non-radiographic intraoperative fluorescent cholangiography is feasible. *Dan. Med. J.* **61**, A4891 (2014).
38. Kaneko, J. et al. Indocyanine green reinjection technique for use in fluorescent angiography concomitant with cholangiography during laparoscopic cholecystectomy. *Surg. Laparosc. Endosc. Percutan. Tech.* **22**, 341–344 (2012).
39. Ishizawa, T. et al. Fluorescent cholangiography illuminating the biliary tree during laparoscopic cholecystectomy. *Br. J. Surg.* **97**, 1369–1377 (2010).
40. Du, T. et al. Hyperspectral imaging and characterization of allergic contact dermatitis in the short-wave infrared. *J. Biophotonics* **13**, e202000040 (2020).

Acknowledgements

This work was supported by the National Key R&D Program of China (2024YFF1206700, J.Q.), the National Natural Science Foundation of China (U23A20487, H.L. and 61975172, J.Q.), and Dr. Li Dak Sum & Yip Yio Chin Development Fund for Regenerative Medicine, Zhejiang University (J.Q.).

Author contributions

J.Q., J.L., and Y.Z. conceived and designed the project. M.Z. performed the synthesis and characterization of probes. J.L., Q.X., and Yixuan Li performed the in vivo experiments. J.L. and Y.Z. performed the imaging experiments. T.W. conducted the simulation. S.P. and Yifei Li ran the integrating sphere test. J.L. performed the imaging analysis and wrote the original manuscript. J.L., T.W., Q.X., J.Q., H.L., and M.Z. wrote and reviewed the manuscript. J.Q. and M.Z. supervised the research.

Competing interests

The authors declare no competing interests.

Additional information

Supplementary information The online version contains supplementary material available at <https://doi.org/10.1038/s41467-025-59630-4>.

Correspondence and requests for materials should be addressed to Mingxi Zhang or Jun Qian.

Peer review information *Nature Communications* thanks the anonymous reviewer(s) for their contribution to the peer review of this work. A peer review file is available.

Reprints and permissions information is available at <http://www.nature.com/reprints>

Publisher's note Springer Nature remains neutral with regard to jurisdictional claims in published maps and institutional affiliations.

Open Access This article is licensed under a Creative Commons Attribution-NonCommercial-NoDerivatives 4.0 International License, which permits any non-commercial use, sharing, distribution and reproduction in any medium or format, as long as you give appropriate credit to the original author(s) and the source, provide a link to the Creative Commons licence, and indicate if you modified the licensed material. You do not have permission under this licence to share adapted material derived from this article or parts of it. The images or other third party material in this article are included in the article's Creative Commons licence, unless indicated otherwise in a credit line to the material. If material is not included in the article's Creative Commons licence and your intended use is not permitted by statutory regulation or exceeds the permitted use, you will need to obtain permission directly from the copyright holder. To view a copy of this licence, visit <http://creativecommons.org/licenses/by-nc-nd/4.0/>.

© The Author(s) 2025